

Review

Intensification of Chemical Looping Processes by Catalyst Assistance and Combination

Hilde Poelman  and Vladimir V. Galvita * 

Laboratory for Chemical Technology, Ghent University, Technologiepark 125, B-9052 Ghent, Belgium; hilde.poelman@UGent.be

* Correspondence: Vladimir.Galvita@UGent.be; Tel.: +32-4-6810-6004

Abstract: Chemical looping can be considered a technology platform, which refers to one common basic concept that can be used for various applications. Compared with a traditional catalytic process, the chemical looping concept allows fuels' conversion and products' separation without extra processes. In addition, the chemical looping technology has another major advantage: combinability, which enables the integration of different reactions into one process, leading to intensification. This review collects various important state-of-the-art examples, such as integration of chemical looping and catalytic processes. Hereby, we demonstrate that chemical looping can in principle be implemented for any catalytic reaction or at least assist in existing processes, provided that the targeted functional group is transferrable by means of suitable carriers.

Keywords: dry reforming; ammonia synthesis; oxygen storage materials; hydrogen production; oxidative dehydrogenation; energy storage; iron; sorption enhanced; super-dry reforming



Citation: Poelman, H.; Galvita, V.V. Intensification of Chemical Looping Processes by Catalyst Assistance and Combination. *Catalysts* **2021**, *11*, 266. <https://doi.org/10.3390/catal11020266>

Academic Editors: Juan J. Bravo-Suarez and Valerie Dupont

Received: 7 January 2021
Accepted: 11 February 2021
Published: 17 February 2021

Publisher's Note: MDPI stays neutral with regard to jurisdictional claims in published maps and institutional affiliations.



Copyright: © 2021 by the authors. Licensee MDPI, Basel, Switzerland. This article is an open access article distributed under the terms and conditions of the Creative Commons Attribution (CC BY) license (<https://creativecommons.org/licenses/by/4.0/>).

1. Concept of Chemical Looping

Currently, there is significant effort to resign our dependence on fossil resources and to minimize the emission of carbon dioxide [1,2]. Clearly, this calls for new and improved catalytic processes and for catalytic technologies that focus on prevention rather than on remediation [3]. To be honest, at present, no efficient technologies exist that enable the use of CO₂ as starting or raw material [4–6]. Such processes could however serve the dual purpose of producing value-added chemicals using CO₂ as a C₁ base chemical and reducing CO₂ emissions. If this were to be carried out at a large scale, say megatons, it would definitely help with mitigating climate change effects by recycling part of the waste CO₂, while creating new opportunities for the chemical industry. What to do? A possible solution can be provided by chemical looping [7–16], a promising technology of low emission, with applications in electricity or heat production, as well as in chemicals and fuels. This novel technology is rapidly evolving towards an established “clean combustion” due to the intrinsic, very efficient CO₂ separation. However, the term chemical looping (CL) is not limited to combustion but can be used in a much broader sense to describe a specific type of reaction scheme. In chemical looping, a conventional catalytic reaction is split in sub-reactions, using intermediates that react and are regenerated in a cyclic way. Based on the type of intermediate, chemical looping processes can be classified in three groups:

1. Chemical looping of redox reactions [8,11–15]. Herein, a metal oxide (MO) acts as oxygen storage material (OSM) (M: reduced form), which takes up oxygen from the oxidant (e.g., H₂O, O₂ or CO₂) and passes it on to the reductant (e.g., C, H₂, CH₄, plastic, etc.) (Figure 1a). By dividing the global reaction in two, the reduced and oxidized products can be separated by running the sub-reactions at two different times or places (temporal or spatial separation). Even solid fuels can be oxidized by appropriate chemical looping materials at a quite reasonable rate. However, the technology of chemical looping is not limited to oxidation only. On the contrary,

combinations of oxygen carriers with other carrier materials can cover a very diverse field of reactions.

- Chemical looping separation of carbon dioxide [8,15–22]. Chemical looping CO₂ separation applies an (earth) alkali metal oxide (MO) as sorbent, to reversibly retain and set free CO₂ (Figure 1b). The process of CO₂ storing is called carbonation because it transforms MO into the corresponding carbonate MCO₃. The opposite process takes place upon heating, thereby releasing the CO₂ (decarbonation). By alternating MO carbonation and decarbonation, CO₂ can be separated from exhaust gases or other dilute streams. The oxygen storage and CO₂ sorbent materials of the processes 1 and 2 can easily be regenerated and hence reused in the next cycle [8,15,18].
- Transfer of surface reaction intermediates by chemical looping (carbon, -OH, S, etc.) between distinct reactions [23,24]. Materials in these chemical looping processes can carry reaction intermediates, which are different from oxygen or CO₂ (Figure 1c). As intermediates form on the surface of the carrier in one step, they are subsequently used in the next. For example, Ni and Zn materials can be used to carry carbon and sulfur, respectively.

The installation of a chemical looping process either requires fixed-bed reactors (number of reactors ≥ 2) (Figure 1d) or alternatively, two interconnected fluidized-bed reactors (Figure 1e).

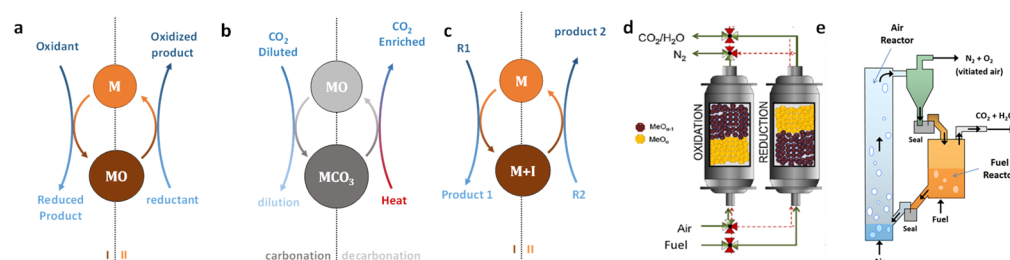


Figure 1. Scheme of some chemical looping processes for: (a) redox reactions and (b) carbon dioxide separation. In (a,b) reduction and decarbonation can equally be achieved by oxygen and carbon dioxide partial pressure decrease, e.g., through an inert gas feed. (c) Chemical looping transfer, where solid materials pass on surface reaction intermediates (carbon, -OH, S,) between separate reactions (R1 and R2). Chemical looping using (d) fixed-bed reactors and (e) two interconnected fluidized-bed reactors.

Considering that it can have various applications, starting from one common basic concept, chemical looping can be considered a true technology platform. Compared to a traditional catalytic process, the chemical looping concept allows to: (i) minimize exergy loss [8,25,26], (ii) intensify the targeted process by combining reaction and separation in a single step [27], (iii) apply H₂O/CO₂ as an oxidant (steam/dry reforming), which enables to produce pure H₂ and CO without the need for downstream separation [8,28,29], (iv) feed lower grade or less pure feedstocks, (v) use cheap materials (CaO, FeO_x) [13,30] and (vi) use fuel without the need for upstream desulfurization [23,31]. A quite notable feature is its ability to provide product separation in situ. Since separation is very energy-intensive, the product separation in chemical looping offers valuable prospects of energy savings and emission reductions.

Next to the above intrinsic qualities, chemical looping has another major advantage: combinability, which allows for integration of different reactions into one process, leading to intensification. Several of the above-mentioned processes are then combined into more advanced chemical looping schemes, such as, e.g., in chemical looping methane reforming enhanced by sorption, or in super-dry reforming, or they are coupled with catalytic reactions, such as, e.g., in catalyst-assisted chemical looping. This review collects various important state-of-the-art examples of such integrations of catalytic processes and chemical looping and the role of multifunctional materials therein.

2. Catalyst-Assisted Chemical Looping

The role that hydrogen plays nowadays in the chemical industry, in parallel to its contribution to energy supply, cannot be underestimated. Currently, hydrogen is mainly used for ammonia production (62%), refining industry (24%), methanol production (8%), metallurgy, in manufacture of high-quality electronic components and in many more applications. There is no doubt that the demand for hydrogen will further rise, both in existing industries and in new technologies like fuel cells [32,33]. A typical process to produce hydrogen comprises methane steam reforming, then water gas shift and a final pressure swing adsorption for purification [34,35]. One or two separate reactors are required for the water gas shift reaction: the high-temperature shift reactor with an iron/chrome catalyst, operating at 350–500 °C. Hereafter, a CO concentration of around 4 mol% on dry basis is present in the outlet stream. To reach a lower CO concentration, a second reactor working at lower temperature is needed. Finally, a preferential oxidation reactor (PROX) or pressure swing adsorption reduces the CO concentration down to the ppm level. The need for such a reactor train means, however, a significant decrease in full process efficiency.

To shorten this conventional production chain, one can consider a chemical looping concept for methane reforming. Such process generates high-purity hydrogen (with carbon oxides at the ppm level) starting from hydrocarbons. Although this is still a two-step process, only a single reactor is required without any post-processing, meaning significant economic profit. Central to this technology are cheap and abundant iron oxide materials, which are to be reduced/re-oxidized periodically, a process in which they transfer oxygen. In the first step, iron oxide gets reduced by methane (or renewable biogas), while the second stage brings the reduced iron back to an oxidized state by feeding steam as an oxidant. Together with the material re-oxidation, hydrogen is being produced.

Obviously, the deeper the oxygen storage material can be reduced, the more hydrogen can be generated upon re-oxidation. In the above process description, reduction of iron oxide, in particular Fe_3O_4 , by methane is slow, so that it limits the attainable degree of reduction [36]. If biogas, a mixture of carbon dioxide and methane, is used as a source of methane, iron oxide reduction is drastically decreased, because it is opposed by carbon dioxide acting as an oxidant [37,38], see Figure 2. Actually, this effect is induced by both feed and product CO_2 , counteracting the iron oxide reduction by methane. To circumvent this drawback, the oxygen storage material bed can be foreseen of a Ni-based catalyst in addition to the iron oxide, either in layers or as physical mixture [39]. The Ni-based catalyst will convert the CH_4 and CO_2 mixture to syngas, i.e., $\text{H}_2 + \text{CO}$, by dry reforming. The latter gases ensure a deeper reduction of iron oxide than with CH_4 . The dry reforming of methane is recently gaining interest as it converts two greenhouse gases as a carbon source. Not only does it produce syngas, which compared to methane has a higher reduction potential, but it also consumes CO_2 from the feed, allowing for deeper reduction of iron oxide, and as a result, for a larger amount of H_2 to be produced in the second re-oxidation step. This is an example of synergy between catalysis over Ni and chemical looping using Fe_3O_4 , in a so-called “catalyst-assisted chemical looping process”.

Chemical looping allows to easily switch between desired products. If in the re-oxidation step steam is replaced by CO_2 as an oxidizing agent, the process turns into chemical looping dry reforming (CLDR). Compared to the conventional form of catalytic dry reforming (DR), CLDR solves some challenges and brings advantages:

- First, removal of deposited carbon: this important issue of DR is solved as carbon will react with CO_2 in every regeneration step of the looping material.
- Second, the use of CO_2 as an oxidant for material regeneration in the re-oxidation allows to convert more CO_2 than in the conventional reaction, namely three times more in CLDR than in DR [40]. As such, the target of chemical looping dry reforming is no longer a high syngas yield as for DR, but rather optimal activation and utilization of CO_2 . A proof of principle for the CLDR process was described by Najera et al. [40]. Based on thermodynamic calculations to select suitable oxygen storage materials,

they synthesized and characterized carriers with nanostructure that showed high activity and stability, showing the potential of the CLDR concept. In addition, reactor modelling evidenced the practical feasibility of the process [40,41].

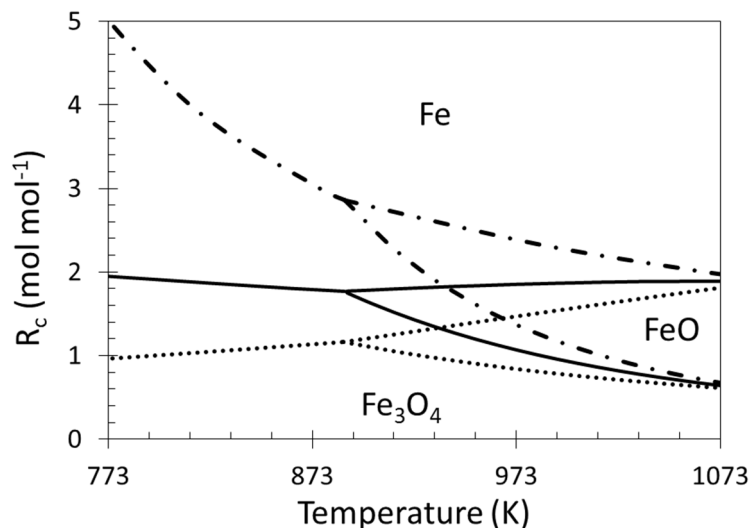


Figure 2. Phase diagram for the equilibrium between iron and its oxides (Fe_3O_4 , FeO and Fe) as a function of temperature and feed gas reduction capacity: $-\cdot-$ $\text{H}_2/\text{H}_2\text{O}$; $-$ $\text{H}_2/\text{CO}/\text{H}_2\text{O}/\text{CO}_2$ (C and H_2 equimolar amount, representing a feed of $\text{CH}_4 + \text{CO}_2$); \cdots CO/CO_2 [38].

The entire concept of the CLDR process stands or falls with the selection of a suitable storage material. Herein, cost, stability and above all reactivity are of the essence. Based on thermodynamic data for reduction and re-oxidation, a wide range of metals/metal oxides were considered [40,42]. While some of these, like Mo, Cr, Zn, Co, Nb and Ce, give reasonable CO_2 conversion capacity, the highest oxygen storage capacity from CO_2 is provided by Fe, namely $0.7 \text{ mol CO}_2/\text{mol}_{\text{Fe}}$, at temperatures $> 600 \text{ }^\circ\text{C}$. This makes CO_2 conversion to CO by chemical looping over an Fe-containing material for oxygen storage a most promising technology. Nevertheless, issues still remain with respect to the process economics, in particular, how to keep up the activity during multiple cycles of reduction/oxidation? Several factors play a role in this. For one, the surface area of FeO influences the reactivity in CO_2 splitting, as found by Loutzenhiser et al. [43]. However, high surface area iron oxides are more susceptible for sintering, an irreversible process, so they rapidly lose activity [44]. The iron oxide lost more than 70% of the initial activity during the first 8 redox cycles. Hence, the viability of the CO_2 conversion process by CLDR, compared to other technologies, can only benefit from iron oxide sintering control during redox cycling to maintain its reactivity. The further optimization of the process thus relies on fundamental studies on the impact of structural and compositional design of the metal oxide and/or catalyst components at the nanoparticle level, as well as of the support on the overall performance.

Catalysts based on Ni are among the most investigated, even given their deactivation by carbon accumulation [45]. They make active and stable catalysts for dry reforming of methane, especially when they are well dispersed. Support materials can help to disperse Ni, and if they have redox properties, like solid solutions or mixed oxides based on ceria, they can also take care of carbon removal. Pure CeO_2 for instance promotes Ni dispersion, while its redox couple $\text{Ce}^{4+}/\text{Ce}^{3+}$ easily gasifies carbon accumulated at the surface by supplying active oxygen. A Ni- CeO_2 /mineral clay catalyst, studied by Daza et al. [46], showed enhanced activity and limited coke formation in methane dry reforming, ascribed to the better dispersion of Ni and improved CO_2 adsorption. Also, Potdar et al. [47] reported about a Ni-Ce catalyst with high surface area showing stable activity and resistance to coke formation in reforming because of high oxygen mobility. In

a similar redox support approach, Ni has been modified with Fe, which also has high redox capacity, just like the Ce species [45]. In this type of design, the support carries both the catalytic and oxygen storage component, making it a multifunctional material. The different functions work together in both steps of the chemical looping dry reforming process: upon reduction, the mixed feed of $\text{CH}_4 + \text{CO}_2$ is converted over Ni to syngas, which reduces both Fe_2O_3 and CeO_2 , thereby producing CO_2 and H_2O . Ni ensures deeper reduction of the oxide materials. In the re-oxidation stage, the reduced material is regenerated by CO_2 to produce CO. The benefit of combining catalyst and oxygen storage functions was obvious as the CO yield turned out to be 10-fold of the one for $\text{Fe}_2\text{O}_3\text{-CeO}_2$ without Ni catalyst [48].

Figure 3 shows the multifunctional 5%Ni/ $\text{Fe}_2\text{O}_3\text{-CeO}_2$ sample in transmission electron microscopy (TEM). The high-resolution image displays crystallites with a size of ~ 17 nm, all bearing a similar morphology (Figure 3a). Energy-dispersive X-ray spectroscopy (EDX)-STEM (Scanning Transmission Electron Microscopy) mapping provided the elemental distribution in the material, showing that Ni (red) prefers to be close to or on the Fe_2O_3 (blue) particles (Figure 3b).

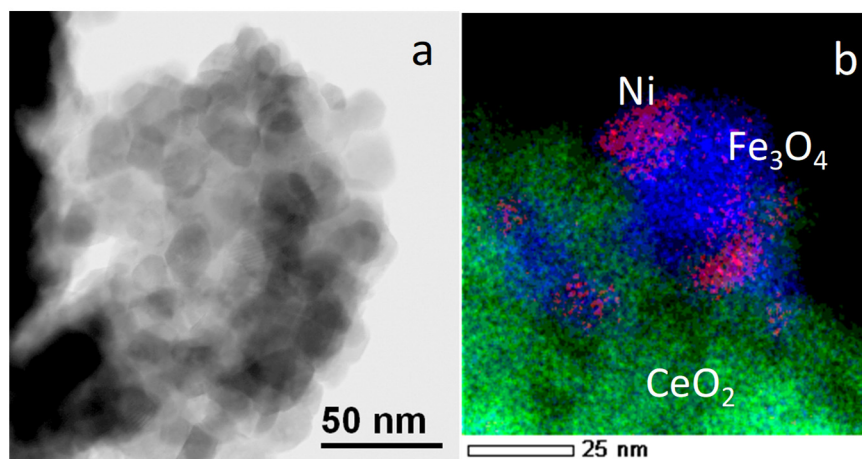


Figure 3. Transmission electron microscopy micrograph of 5%Ni/ $\text{Fe}_2\text{O}_3\text{-CeO}_2$ (a) and (b) higher magnification to show the energy-dispersive X-ray spectroscopy (EDX) element mappings of Fe (blue), Ce (green) and Ni (red), close to each other [48].

Together with DR, side reactions can occur depending on the operating temperature and partial pressure of the reactants. These comprise CH_4 decomposition (Equation (1)) as well as the Boudouard reaction (Equation (2)), where CO transforms into surface carbon and CO_2 :



Re-oxidizing the reduced Ni/ $\text{Fe}_2\text{O}_3\text{-CeO}_2$ with CO_2 , while applying in situ X-ray diffraction (XRD), yields interesting details. A set of patterns was recorded during a few oxidation/inert/dry reforming cycles at 873 K (Figure 4). Reaction temperature was reached with a high heating rate up to 873 K, temperature which was then maintained. Depending on the gas environment present throughout the chemical looping experiment, He, CO_2 or $\text{CO}_2 + \text{CH}_4$, the background intensity of the whole pattern varied because of differences in X-ray scattering. The first reduction treatment under $\text{CH}_4 + \text{CO}_2$ forms Fe with main diffraction at 45° and the Ni_3Fe alloy after 100 s. Upon introduction of CO_2 into the reactor after 5 min, Fe is converted to FeO and further to Fe_3O_4 . At the same time, the Ni_3Fe alloy phase loses some intensity, and formation of a small amount of NiFe_2O_4 spinel cannot be excluded. Diffractions for this spinel would yield shoulders to the Fe_3O_4 diffractions, but for this material, they likely remain undetected as the Ni loading in the sample is very small. The Fe_3O_4 phase appeared stable under CO_2 and also shortly

thereafter, already under He. However, while still under inert flow, the Fe_3O_4 peaks started fading and changed back into FeO and Fe diffractions as if again reduced. Simultaneously, the alloy phase diffraction became more intense. A second CO_2 period reconverted FeO and Fe to Fe_3O_4 , which then persisted throughout the entire 7 min of He flow. At the origin of these observations is carbon, formed during the reduction step and accumulated on the catalyst surface.

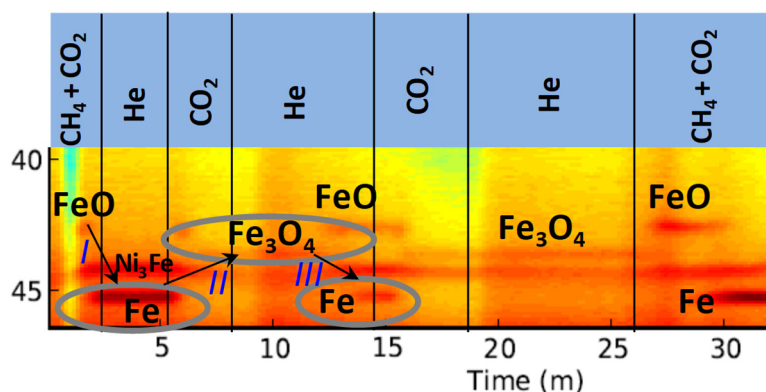


Figure 4. In situ XRD patterns collected from Ni/Fe₂O₃–CeO₂ during reduction/oxidation cycles at 873 K. Transitions are indicated by arrows: FeO reduction (I) and re-oxidation (II), disappearing Fe₃O₄ diffraction, re-emergence of first FeO and then Fe in He flow after CO₂ re-oxidation (III). Gas environments are indicated above the two-dimensional (2D) patterns [48].

The in situ XRD interpretation is as follows: When introducing pure CO₂ for the first time after reduction, it re-oxidizes iron and CeO_{2- δ} , thereby replenishing their lattice oxygen. The latter then oxidizes the surface carbon. In principle, carbon could also be oxidized directly by CO₂ according to the Boudouard reaction. However, this cycling in situ XRD experiment proves that oxidation of carbon deposits by lattice oxygen equally occurs, since even under inert flow, iron oxide is again reduced (Figure 4, step III). Apparently, the first CO₂ pulse was not sufficiently long to both re-oxidize the material and remove all carbon from the surface. As a result, after the CO₂ pulse, the remaining C gets removed with the help of lattice oxygen from the Fe₂O₃–CeO₂ material, leading to reduction anew even without a reductive atmosphere. The subsequent longer CO₂ pulse removes all carbon so that Fe is permanently oxidized back to Fe₃O₄.

The duration of the catalytic activity and hence the extent of carbon formation on the surface depend on the overall oxygen capacity of the material. Usually, coke formed on the catalyst surface is responsible for fouling of the active sites, thereby deactivating the nickel catalyst particles. In order to counter this, the material requires periodic regeneration, which is exactly what the concept of chemical looping is providing, since it comprises cycles of reduction and re-oxidation steps. The refill of the OSM upon re-oxidation is conveniently accompanied by surface carbon removal, which in parallel yields more CO than the theoretical value which stems from complete oxidation of Fe to Fe₃O₄.

Another example of a catalyst-assisted chemical looping process is steam reforming of methane (CLSRM), which is capable of generating both syngas and hydrogen in its half-cycles [49]. Whereas in the previous example, Ni was taking up the catalyst function, here, Fe₂O₃ and/or CeO₂ fulfil this role. The used Fe@Ce material with core-shell architecture is key to this process. Using a ceria shell enclosing an iron oxide core as an oxygen carrier combines advantages of ceria and iron oxide: high ion conductivity for the former and high oxygen storage capacity for the latter. The activity of Fe@Ce was assessed in fixed-bed tests and compared to a uniform mix of Fe–Ce as a reference. Compared to the mixture, the core-shell Fe@Ce material yielded more syngas and hydrogen, and better selectivity for CO and methane conversion in the reduction process. The syngas and hydrogen yield of Fe@Ce was an approximately constant value of 16 and 6 mmol \times g⁻¹ compared to 14

and $5 \text{ mmol} \times \text{g}^{-1}$ for the CeO_2 and Fe_2O_3 mixture. This indicates that the core-shell structure can selectively provide oxygen from the CeO_2 shell, which eases the transport of oxygen ions between the core and the shell. Moreover, the selectivity to CO and the CH_4 conversion for the core-shell oxygen carrier further improved for an increasing number of cycles, likely due to the enhancement of the oxygen ion conduction and resulting from the increasing contribution of a CeFeO_3 phase. The carbon deposition for Fe@Ce amounted on average to only 29% of that for Fe-Ce , leading to higher-quality syngas with a H_2/CO ratio close to 2 and higher-purity H_2 . The high resistance against C accumulation was ascribed to the ceria shell, having excellent oxygen ion conductivity. The latter ensures rapid migration and replenishment of oxygen ions at the surface. In addition, iron metal sites, which activate methane, are scarce on the surface, due to the CeO_2 shell, leading to higher carbon resistance.

CeO_2 itself is quite active towards methane oxidation through its lattice oxygen, and it has a reasonable capacity for H_2O or CO_2 re-oxidation [50,51]. Oxygen storage in and release from the bulk fluorite lattice are facilitated by its redox couple Ce^{4+} and Ce^{3+} . In combination with iron oxide, CeO_2 can modify and stabilize the structure, making it very suited as a promoter of iron oxide in a chemical looping process. When combining CeO_2 with MeO_x ($\text{Me} = \text{Mn}, \text{Fe}, \text{or Cu}$), a mixed oxide was formed, exhibiting higher reducibility than pure CeO_2 [52,53]. When CeO_2 interacts with Fe_2O_3 , this also leads to enhanced reducibility of Fe_2O_3 [54]. Depending on the composition, part of the interaction is established through formation of a mixed oxide, wherein the ceria structure takes up a limited amount of Fe^{3+} cations. The evolution of the Fe_2O_3 - CeO_2 structure as a function of composition is shown in Figure 5 [53].

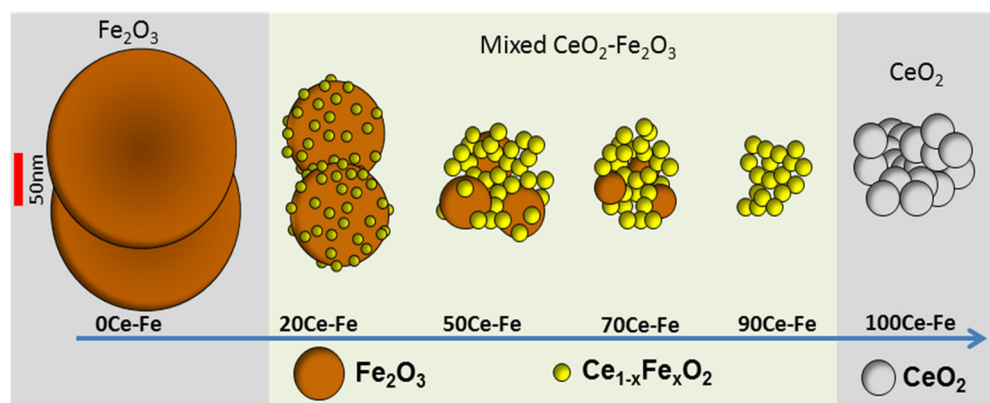


Figure 5. Scheme of a series of mixed CeO_2 - Fe_2O_3 samples, composed on the basis of inductively coupled plasma (ICP) composition, XRD, STEM, EDX and EELS analysis [53].

The question is how much Fe can actually be incorporated into ceria for different compound ratios? The CeO_2 lattice parameter for the entire range of mixed oxide materials (Figure 6) levels off beyond 10 wt% Fe_2O_3 - CeO_2 [54]. In addition, the XRD pattern for 10 wt% Fe_2O_3 - CeO_2 shows no Fe_2O_3 contribution, meaning no separate crystalline phase is present, unless it is nanosized. In order to assess this maximal Fe amount in the lattice, the Ce-K edge Extended X-Ray Absorption Fine Structure (EXAFS) signal for 10 wt% Fe_2O_3 - CeO_2 was recorded and fitted. Two models were compared for the fit: one for the pure CeO_2 fluorite structure and another one with a Fe-doped CeO_2 structure or solid solution, denoted as $\text{Ce}_{1-x}\text{Fe}_x\text{O}_{2-x}$, where x denotes the incorporated amount of Fe, taken as a parameter in the fit. A value of $x = 0.21 \pm 0.08$ yielded the best correspondence (Figure 7), meaning that 21% of the Ce atoms in CeO_2 are substituted by Fe. For 10 wt% Fe_2O_3 - CeO_2 , this number indicates that 85% of the Fe forms a solid solution with ceria as $\text{Ce}_{1-x}\text{Fe}_x\text{O}_{2-x}$. As the ceria lattice parameter does not change beyond 10 wt% Fe_2O_3 , it can be safely assumed that, e.g., in 80 wt% Fe_2O_3 - CeO_2 , the same 21 mol% of Ce is exchanged for Fe, which of course represents only a small fraction of all Fe in 80 wt% Fe_2O_3 - CeO_2 .

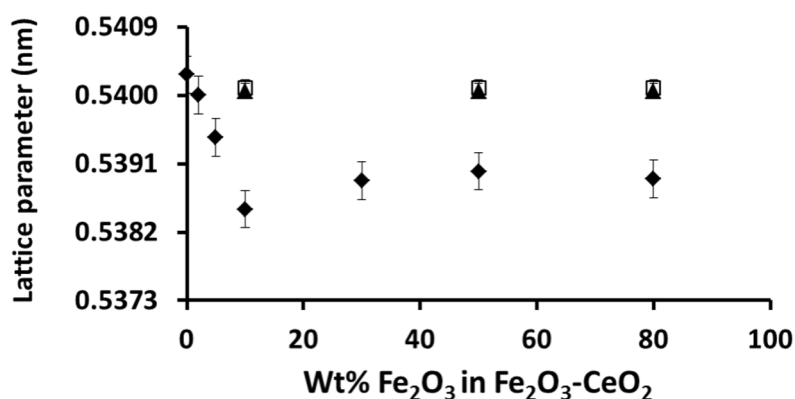


Figure 6. Unit cell parameters for ceria in a series of x wt% Fe₂O₃-CeO₂ with variable Fe₂O₃ loading (diamond) as prepared, (triangle) CO₂-reoxidation and (square) O₂-reoxidation states. Error bars represent standard deviation (68% confidence interval) [54].

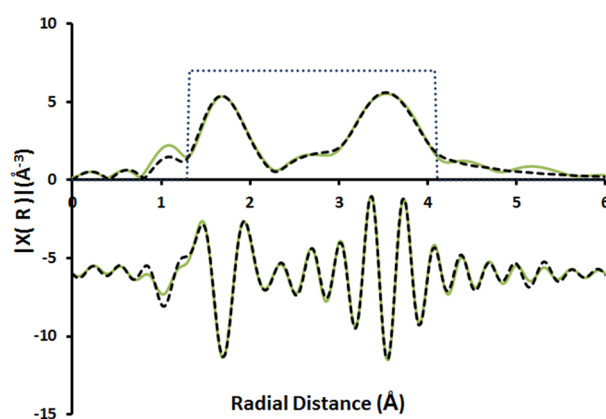


Figure 7. Fourier-transformed k^2 -weighted Ce-K edge Extended X-Ray Absorption Fine Structure (EXAFS) spectrum for 10 wt% Fe₂O₃-CeO₂ and modelling fit (dashed line), with an Fe incorporated CeO₂ model Ce_{1-x}Fe_xO_{2-x}, wherein $x = 0.21$. Upper part: Fourier transforms (FT) modulus, lower part: imaginary Im[FT[$k^2 \chi(R)$]]. Dotted rectangle: window fitting range. No phase correction was used. (—) EXAFS signal of 10 wt% Fe₂O₃-CeO₂, (---) fit and (····) fitting window [54].

To identify the structural properties of Fe-rich material at the far end of the Fe₂O₃-CeO₂ mixing range, 80 wt% Fe₂O₃-CeO₂ was also investigated. Figure 8a shows a high angle annular dark field scanning TEM (HAADF-STEM) image for 80 wt% Fe₂O₃-CeO₂, in which two types of particles are discerned: small ones, decorating larger ones. According to Electron energy loss spectroscopy (EELS) maps, the former are CeO₂ (Figure 8b), while the latter pertain to Fe₂O₃ (~50 nm). After 100 cycles of chemical looping, the particles are strongly agglomerated, and show considerably larger size (Figure 8c). Nevertheless, even in this sintered condition, the decorative configuration of ceria surrounding iron oxide persists (Figure 8d).

For the above-mentioned Fe₂O₃-CeO₂ materials, the crystalline phases, sizes and morphological changes, before and after cycled operation (as in chemical looping), were determined using (S)TEM, XAS (X-ray absorption spectroscopy) and XRD. Next to sintering, two other types of deactivation were identified: first, Fe can get extracted from the Ce_{1-x}Fe_xO₂ solid solution, and second, a perovskite (CeFeO₃) can be formed. The extraction of Fe from the solid solution can proceed quite fast, leading to less reducibility for CeO₂. However, the extraction sets free more Fe, which in turn can add to the overall oxygen storage capacity. For the latter, perovskite formation is only negative, as CeFeO₃ is not reducible below 800 °C. The slowest deactivation process is undoubtedly sintering,

occurring throughout operation. Because it steers crystallite sizes to grow, longer diffusion times are induced for oxygen to move from the bulk to the surface. So, a given reduction time will gradually lead to a lower degree of reduction reached, hence less CO yield upon re-oxidation.

Which of these deactivation types dominates is dependent on the material composition. Iron-rich samples are mostly prone to sintering as a predominant mechanism, while Fe extraction is less important based on composition. Similarly, there could be some perovskite forming, but its contribution to the overall composition will not affect the productivity. For ceria-rich samples, all three types of deactivation need to be taken into account. Looking at the CO yield, the best performing material for extended use in chemical looping is 80 wt% Fe_2O_3 - CeO_2 . In this sample, sintering as a main deactivation mechanism is controlled by decorating Fe_2O_3 with CeO_2 nanoparticles.

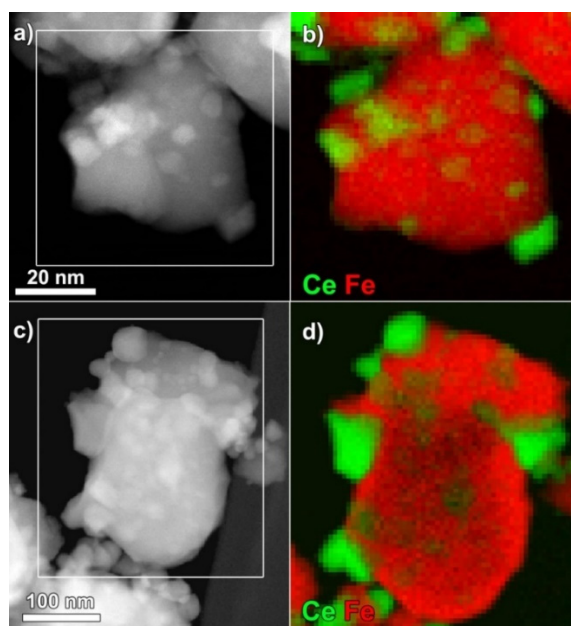


Figure 8. (a) Image of calcined 80 wt% Fe_2O_3 - CeO_2 via high angle annular dark field scanning TEM (HAADF -STEM), (b) corresponding EELS map for Fe and Ce, (c) image for cycled 80 wt% Fe_2O_3 - CeO_2 (100 H_2 - CO_2 redox cycles) and (d) corresponding EELS map for Fe and Ce [54].

When looking for materials that combine a catalytic (A) with an oxygen storage function (Fe), spinel ferrites with composition AFe_2O_4 also come into the picture. Unlike modifying a Fe-based material by adding a catalyst, ferrite-based materials are prepared via co-precipitation of all elements. Among a series of chemical looping experiments with Me-ferrites (Me = Ni, Co, Cu, Mn, Zn), interesting CH_4 dry reforming activity and redox stability were found for NiFe_2O_4 and CoFe_2O_4 . As biomass conversion increases the availability of alcohols as possible feedstock, these two bifunctional materials were then tested for chemical looping alcohol reforming with ethanol and methanol into syngas. NiFe_2O_4 - CeZrO_2 and CoFe_2O_4 - CeZrO_2 were studied by Dharanipragada et al. [55] as bifunctional materials for catalyst-assisted chemical looping dry reforming (CCDR) with either a pure methanol feed or a mixed ethanol-water feed (1:1 molar ratio). The alcohols are fed in the chemical looping reduction step, where they are converted over the catalyst to CO and H_2 , aside from some CH_4 in case water is co-fed. These gases reduce the oxygen storage component of the material, so that in the subsequent re-oxidation step, its regeneration with CO_2 produces CO (Figure 9).

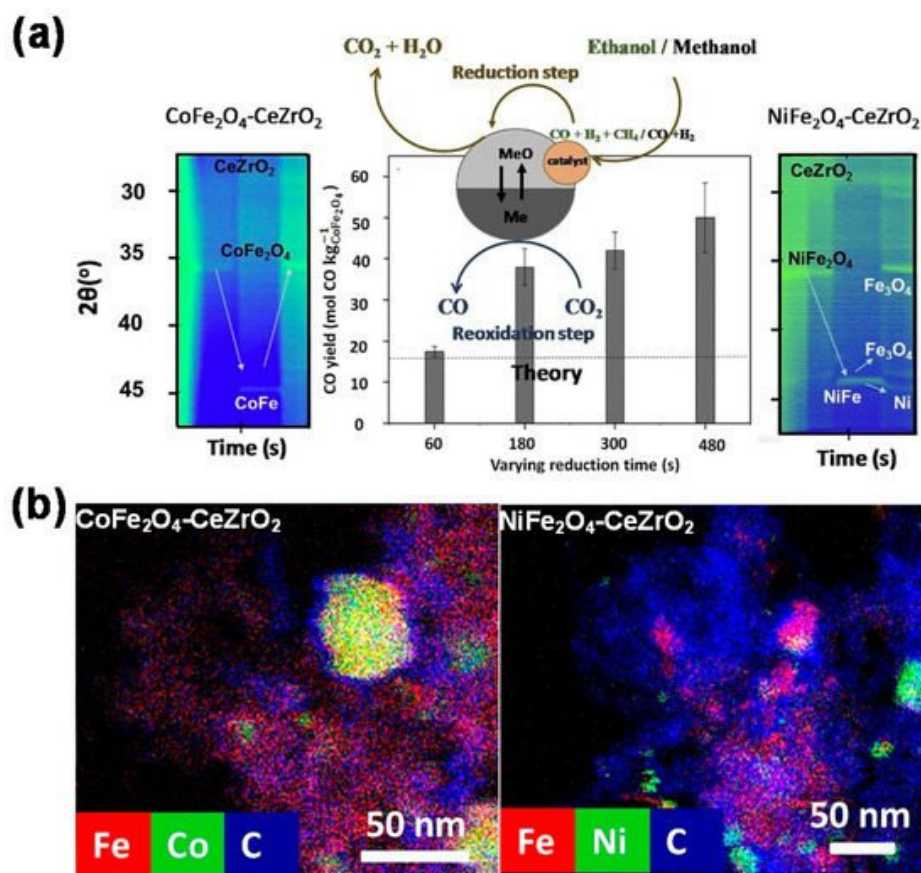


Figure 9. Bifunctional Co- and Ni-ferrites modified with CeZrO₂ for chemical looping dry reforming with alcohols as feed: (a) Transformation of solid and gaseous phases, (b) elemental maps of Co, Ni, Fe and C in 20 wt% CoFe₂O₄-CeZrO₂ and NiFe₂O₄-CeZrO₂ after methanol redox cycles [55].

Material with low CoFe₂O₄ content (20 wt%) presented good redox activity and stability, while the 80 wt% CoFe₂O₄-loaded material deactivated, due to Co and Fe₃O₄ segregation from the ferrite. As for the Ni-ferrite-CeZrO₂ materials, these were all prone to sintering and phase segregation, which turned out to be irreversible. Carbon formation was observed in the methanol-based CCDR process for both types of ferrite materials, but far more over the Ni-ferrite (Figure 9b), demonstrating a significantly lower carbon resistance. As mentioned before, the presence of carbon deposits can enhance the CO yield upon re-oxidation with CO₂, raising the yield above the theoretical value, as was verified experimentally (Figure 9a).

Materials, having dual functions of catalyst and oxygen storage, perform well in catalyst-assisted chemical looping. Based on the latter behavior, autothermal catalyst-assisted chemical looping with the same materials has been advanced as a novel strategy for CO production from CH₄ and CO₂ [56]. The process is built on two approaches, each with a dedicated material: 1/Fe₃O₄ for CO production by chemical looping and 2/a Ni-based catalyst for autothermal catalytic conversion of CH₄, CO₂ and O₂ to syngas. The design of the process allows to convert three times as much CO₂ than is produced in the reduction. By feeding CH₄, CO₂ and, in addition, some O₂, simultaneously to the chemical looping reactor, the endothermicity of dry reforming is overcome. According to thermodynamic analysis, a molar ratio of CH₄/O₂ equal to 0.3 or 0.5 allows to achieve autothermal operation at 873 and 1023 K, respectively. If the ratio of reducing (CO + H₂) to oxidizing (H₂O + CO₂) gases in the feed during the reduction is above 2 and the temperature over 873 K, a high degree of Fe₃O₄ reduction can be obtained. To prove this concept, a multifunctional 9 wt% NiO-16 wt% Fe₂O₃/MgAl₂O₄ was synthesized to test the

process. In the reducing step, $\text{CH}_4 + \text{CO}_2 + \text{O}_2$ (molar ratio of 1:1:0.5) is converted by the NiO catalyst into a CO and H_2 mixture, which reduces Fe_3O_4 , producing CO_2 and H_2O . At the same time, reduction induces interaction between Ni with Fe so that a Ni-Fe alloy is formed. Subsequent CO_2 feeding leads to decomposition of the alloy into Ni and Fe_3O_4 , in parallel to CO production by re-oxidation of reduced iron oxide. Although deactivation occurs for all materials during extended operation at 1023 K, principally due to sintering according to TEM imaging, the latter seems to be limited mainly to the first few cycles, after which operation stabilizes [56].

Recently, calcium ferrite $\text{Ca}_2\text{Fe}_2\text{O}_5$ has been explored as an oxygen carrier for chemical looping and this material can reportedly provide a higher steam conversion to hydrogen than Fe_2O_3 [57–60]. However, the system has limited reactivity with CH_4 . High-purity H_2 can however be produced from CH_4 using approaches based on catalyst-assisted chemical looping. Hosseini et al. demonstrated that doping calcium ferrite with Ni or Cu significantly enhances their redox performance [61]. It was found that adding Cu to $\text{Ca}_2\text{Fe}_2\text{O}_5$ increases the reducibility with CH_4 and yields stable H_2 production. They also showed that copper has high incorporation mobility in the material during air re-oxidation, which provides an effective way to control the Cu nanoparticles' dispersion. Such exsolution and re-incorporation of copper is key to maintain the high reactivity. In contrast to Cu, Ni-doped calcium ferrite did not provide stability in H_2 production. In situ XRD and STEM-EDS identified that during material reduction, a Ni-Fe alloy formed, which may lead to gradual sintering of Ni particles [61].

The same strategy of reversible exsolution to control dispersion of metallic nanoparticles was used by Carrillo et al. [62–64]. $\text{La}_{0.6}\text{Sr}_{0.4}\text{Cr}_{0.8}\text{Co}_{0.2}\text{O}_3$ (LSCC) was selected as an oxygen carrier for CO_2 conversion into CO. The perovskite was promoted with Co nanoparticles for the methane reforming reaction. The 30 nm Co nanoparticles exhibited microstructural stability and uniform dispersion during 28 redox cycles at 900 °C.

Ethylene makes an important building block and valuable commodity chemical for many compounds such as oxygenates, polymers and other chemical intermediates. It is mainly produced by steam cracking, for which ethane oxidative dehydrogenation (ODH) could be an alternative [65–67]. Herein, hydrogen is oxidized with oxygen, so that the ethane conversion equilibrium is shifted, and the overall reaction becomes exothermic. However, ethane ODH faces some practical challenges: (i) potential safety hazards arise when cofeeding oxygen and ethane, requiring dilution with inert gas, (ii) separating air for oxygen generation is capital- and energy-intensive and (iii) ethylene selectivity is reported to be limited at high single-pass ethane conversions.

To overcome these challenges, it was proposed by Gao et al. [68] to use oxidative dehydrogenation in a chemical looping manner (CL-ODH) (see Figure 10) [69]. In this concept, CL-ODH resembles chemical looping redox processes, like oxygen uncoupling (CLOU) [70] and methane partial oxidation [71]. In CL-ODH, oxygen is delivered from the lattice of a redox catalyst to convert ethane to ethylene and water. The ODH drawbacks are then circumvented as air separation is not required, which removes the safety issues about mixing ethane with oxygen. Based on process simulations, the CL-ODH process leads to a reduction of CO_2 emissions by up to 82% when compared to steam cracking, and less energy consumption. Mg_6MnO_8 promoted with sodium tungstate (Na_2WO_4) was shown to be an effective redox catalyst for CL-ODH. In order to achieve high ethylene selectivity, both Na and W were found to be necessary to form Na_2WO_4 . With a Na:W ratio lower than 2:1, additional mixed tungsten oxide phases are formed, which leads to less ethylene selectivity.

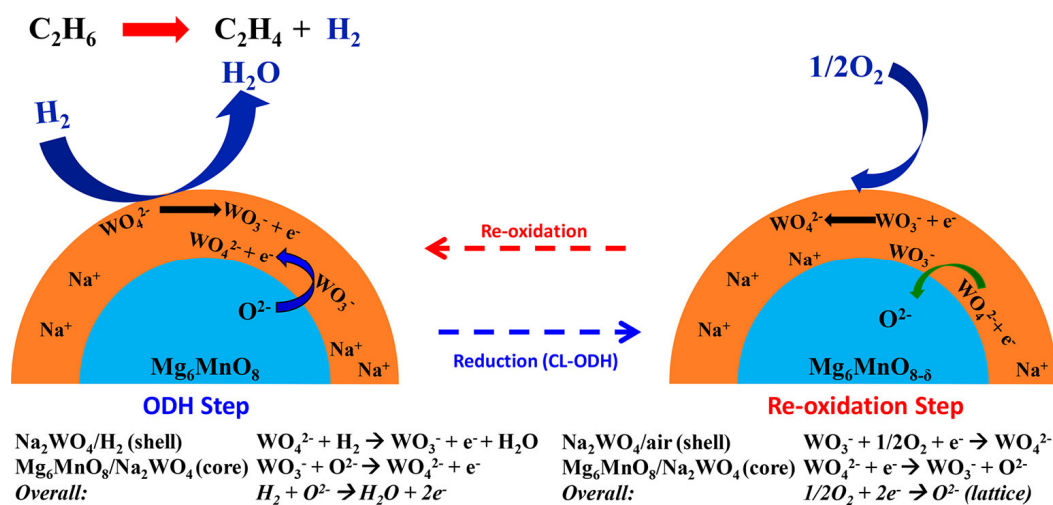


Figure 10. Scheme for oxidative dehydrogenation in a chemical looping manner of ethane over Mg_6MnO_8 redox catalysts, promoted with NaW (In each step, reduction/oxidation of Mn cations in the Mg_6MnO_8 core balance the electrons) [69].

An interesting process for methane conversion from stranded natural gas to valuable liquid aromatic compounds is provided by dehydroaromatization (DHA), a reaction which is limited by thermodynamics. Brady et al. [72] have presented a way to overcome this limitation by placing DHA in a chemical looping frame to enable reactive separation of H_2 from the DHA products. They proposed a four-step cycle to achieve this: DHA over a Mo/H-ZSM-5 catalyst, removal of H_2 , $\text{Fe}_3\text{O}_4/\text{FeO}$ redox pair regeneration and water removal on H-ZSM-5. Each of these steps was evaluated individually, to assess the process feasibility, and the results indicate that the proposed process allows to achieve an aromatics yield of over 40%.

It is still a challenge to control selectivity in partial oxidation of methane by lattice oxygen of metal oxides. Zvang et al. present the finding that distortion of FeO_6 octahedra in $\text{La}_{1-x}\text{Ce}_x\text{FeO}_3$ perovskites positively affects the surface oxygen exchange capability and mobility of bulk oxygen [73]. The distortion of the FeO_6 octahedra can be promoted due to the difference between Ce–O and La–O bond lengths. The authors achieve a syngas productivity during the reduction cycle of 3 to up to 8 times higher than with LaFeO_3 and CeFeO_3 . At the same time, a CO_2 conversion of 92% was achieved during the re-oxidation cycle. Adjusting the octahedral distortion in these perovskites hence provides a means to modulate the active lattice oxygen, which affects their performance in chemical looping processes.

Catalyst-assisted chemical looping processes can also aim at N_2 activation and conversion, wherein hydrogen species play a role, as highlighted in a recent publication [74]. Herein, ammonia is advanced as a promising “carbon-free” energy carrier, but its current industrial synthesis requires severe conditions. If it could be produced at lower temperatures and pressures, this would drastically increase its prospects as an energy carrier and chemical alike. Both alkali and alkaline earth metal imides can operate as nitrogen carriers and produce ammonia via a chemical looping process, operating at atmospheric pressure and 100 °C, according to Gao et al. [74]. The first step fixes nitrogen into imides by reduction with alkali or alkaline earth metal hydrides. The second step hydrogenates the imides to produce NH_3 , thereby regenerating the metal hydrides. Throughout this process, the hydrogen oxidation state switches between -1 (hydride), 0 (H_2) and $+1$ (imide and NH_3) (see Figure 11). This scheme for NH_3 production is mediated by BaNH and catalyzed by Ni, making it another example of a catalyst-assisted chemical looping process.

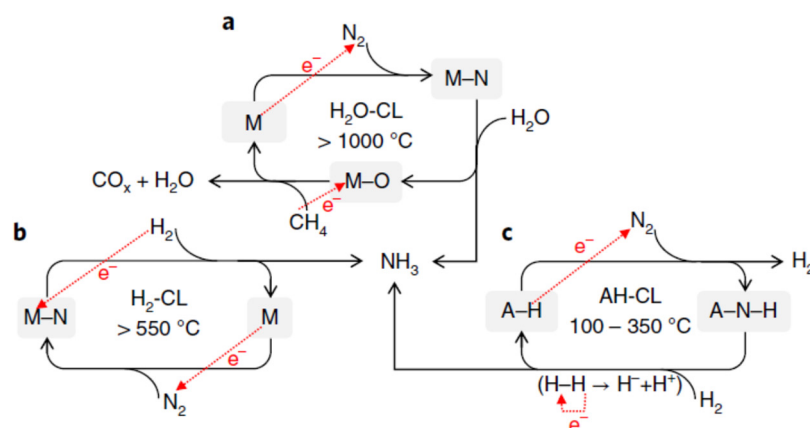


Figure 11. Ammonia synthesis by catalyst-assisted chemical looping: (a) H₂O-CL process, (b) H₂-CL process, (c) AH-CL process. Metal and the corresponding metal nitride and oxide are represented by M, M-N and M-O, respectively. A-H and A-N-H stand for alkali or alkaline earth metal hydride and imide, respectively [74].

Figure 12 presents the rates of ammonia production in chemical looping and catalyst-assisted processes using Ni. The loop with neat LiH/Li₂NH as a mediator produces ammonia at a rate of $\sim 100 \mu\text{mol NH}_3 \text{ g}^{-1}_{\text{LiH}} \text{ h}^{-1}$ at 350 °C, while the 50% Ni-LiH sample achieves $1530 \mu\text{mol NH}_3 \text{ g}^{-1}_{\text{LiH}} \text{ h}^{-1}$ at 300 °C. At that same temperature, neat BaH₂/BaNH used in a loop produces $200 \mu\text{mol NH}_3 \text{ g}^{-1}_{\text{BaH}_2} \text{ h}^{-1}$, though a much higher value of $3120 \mu\text{mol NH}_3 \text{ g}^{-1}_{\text{BaH}_2} \text{ h}^{-1}$ is accomplished by 50% Ni-BaH₂. Even 5% Ni addition can boost the NH₃ production rate from BaH₂-CL six-fold.

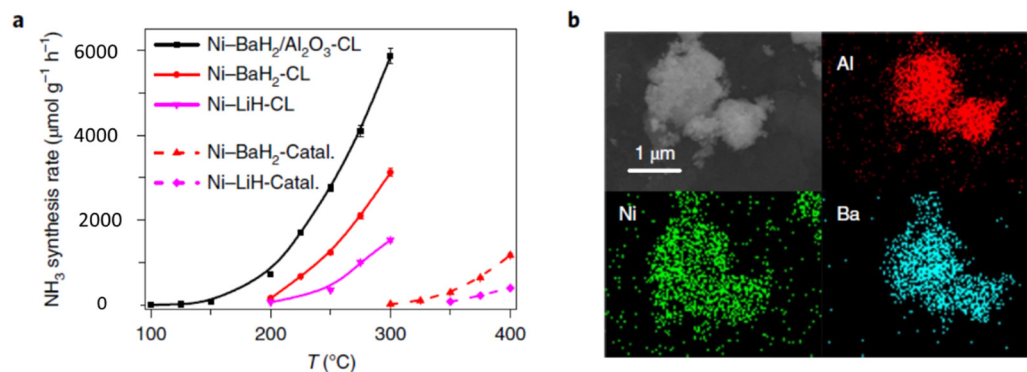


Figure 12. Ni-BaH₂ and Ni-LiH performance in NH₃ production. (a) Temperature-dependent production rates in chemical looping (CL) and thermo-catalytic processes (Catal). (b) Microscope images and elemental maps of spent Ni-BaH₂/Al₂O₃ [74].

3. Combined Chemical Looping

Integrating several processes into one overall scheme of combined chemical looping (CCL) has multiple advantages. As an example, sorption-enhanced steam reforming (SESR), advanced by Lyon and Cole [75], lowers the economic and environmental barriers that accompany conventional reforming, while offering high efficiency, autothermal operation, together with inherent separation of pure H₂ and CO₂ (Figure 13a) [19,76,77]. The exothermicity of the oxygen carrier re-oxidation supplies energy for the endothermic reaction of sorbent regeneration, so that heat requirements are minimal. According to thermodynamic calculations, a decrease of up to 55% in energy demand is possible compared to the conventional steam reforming process [78]. Production of high-purity H₂ and pure CO₂ as by-products, with a high degree of autothermicity, was equally demonstrated by Lemonidou's group. They mixed NiO/ZrO₂ and CaO/CaZrO₃ with NiO/CaO = 0.5 in a

fixed-bed reactor [79–81] to run the process, which combines catalytic steam reforming, calcium chemical looping and chemical looping combustion. Figure 14 displays the reformat gas composition on dry basis during the reduction/reforming step. The H_2 yield during combined chemical looping steam reforming lies very close to equilibrium. As more and more product CO_2 is taken up by the sorbent, the more the concentrations of CO , CO_2 and CH_4 start to increase at the expense of H_2 production (BT: breakthrough). When the sorbent is completely saturated (Post-BT: post-breakthrough), the capture of CO_2 stops, and the outlet gas composition equals the one for conventional steam reforming at these conditions. This is the time for switching the gas feed to air in order to re-oxidize Ni and release the CO_2 from the sorbent. The temperature profile and CO_2 release during this re-oxidation-calcination stage are depicted in Figure 14c, along with a picture where the measuring positions of temperature are marked. No additional heating was applied after introduction of air, as there was sufficient heat stemming from Ni re-oxidation to raise the temperature of the reactor from 650 to ~ 800 °C (Figure 14c). The latter then facilitated the calcination of the sorbent, as evidenced by the CO_2 production. When the Ni oxidation comes to an end, the reactor temperature starts to drop with a concomitant decline in the CO_2 formation rate. In a practical application, so the authors remark, the heat from Ni re-oxidation could even be better utilized if materials were to be moved to another regeneration reactor, where they could be kept at high temperature.

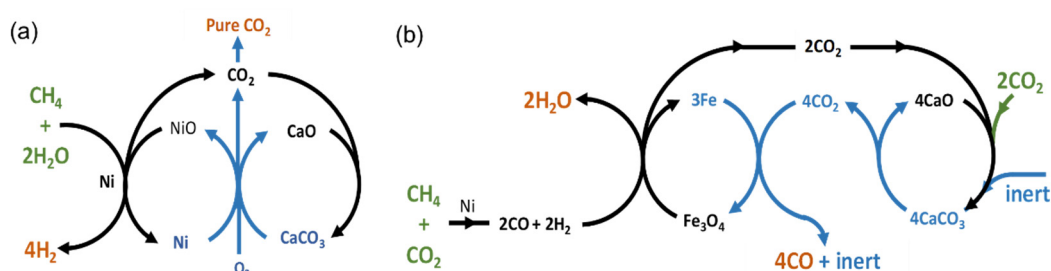


Figure 13. Schemes of combined chemical looping processes: (a) Sorption-enhanced chemical looping reforming of CH_4 , black arrows: NiO reduction, H_2 production by CH_4 reforming and water gas shift over Ni catalyst, carbonation, blue arrows: Ni oxidation, decarbonation. (b) Super-dry chemical looping reforming of CH_4 , black arrows: CO_2 reforming over Ni catalyst, FeO_x reduction, carbonation, blue arrows: decarbonation, CO production by Fe oxidation.

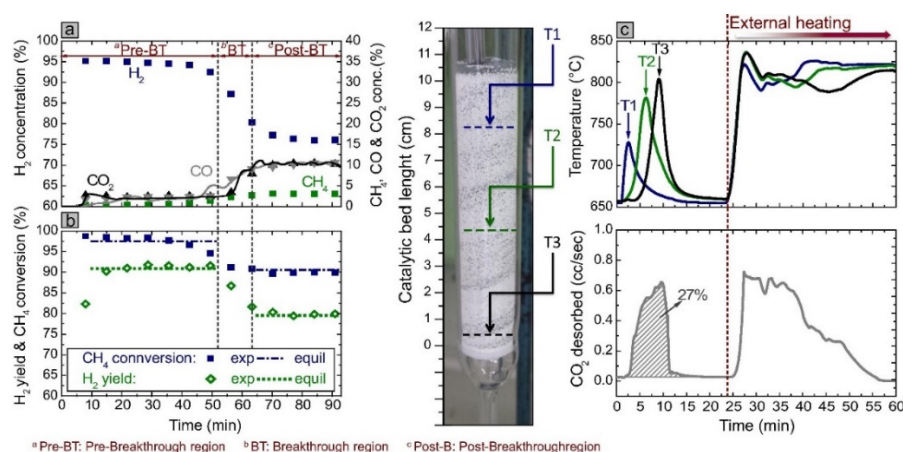


Figure 14. (a) Outlet concentrations, and (b) yield of H_2 and CH_4 conversion versus time during reduction-steam reforming-carbonation. (c) CO_2 formation and temperature profiles versus time during re-oxidation/calcination (reduction-reforming-carbonation: $T = 650$ °C, Steam/Carbon ratio = 3, NiO/CaO molar ratio = 0.5, $GHSV = 250$ h^{-1} ; T during regeneration: $650 \rightarrow 800$ °C, air flow, $GHSV = 430$ h^{-1}) [80].

As mentioned above, the catalytic reaction of CH_4 with CO_2 or methane dry reforming (DRM) also benefits from the chemical looping concept. Recently, it was intensified in super-dry reforming (SDR), a process designed for intensified CO production from CH_4 and CO_2 [38,82]. Three different materials are needed for this process, each with a particular function: $\text{CaO}/\text{Al}_2\text{O}_3$ as a CO_2 sorbent, $\text{Fe}_2\text{O}_3/\text{MgAl}_2\text{O}_4$ to transfer oxygen and $\text{Ni}/\text{MgAl}_2\text{O}_4$ as a CH_4 reforming catalyst, complemented with CH_4 and CO_2 in a 1:3 ratio (Figure 13b). Here, the exothermicity of CaCO_3 formation is coupled to two endothermic processes, CH_4 reforming and Fe_3O_4 reduction, whereby the energy requirement is looped. The isothermal connection between these three processes results in higher CO production than with conventional dry reforming.

The most important asset of the calcium looping and methane reforming process as proposed lies in merging the capture of CO_2 and its subsequent conversion inclusively in one combined process [83]. Figure 15a illustrates such operation, operating with a CaO-Ni multifunctional sorbent-catalyst. In the CO_2 capture step, the CaO component selectively adsorbs CO_2 from the feed stream and stores it as CaCO_3 .

In the CO_2 conversion and CH_4 reforming step, CaCO_3 dissociates to release CO_2 , which is used in situ for reforming of CH_4 on the Ni catalyst, so that syngas is produced. Hereafter, the material is back in its initial state, all set for a new cycle. An essential benefit of this process is that it can use feedstocks with any composition of CO_2 -containing gas to react with CH_4 , in particular flue gases with a CO_2 content of up to 20 vol.%. The integration of CO_2 capture and conversion in one process lowers the overall energy penalty by the improved process heat management and by taking out CO_2 transport from emission point to utilization site.

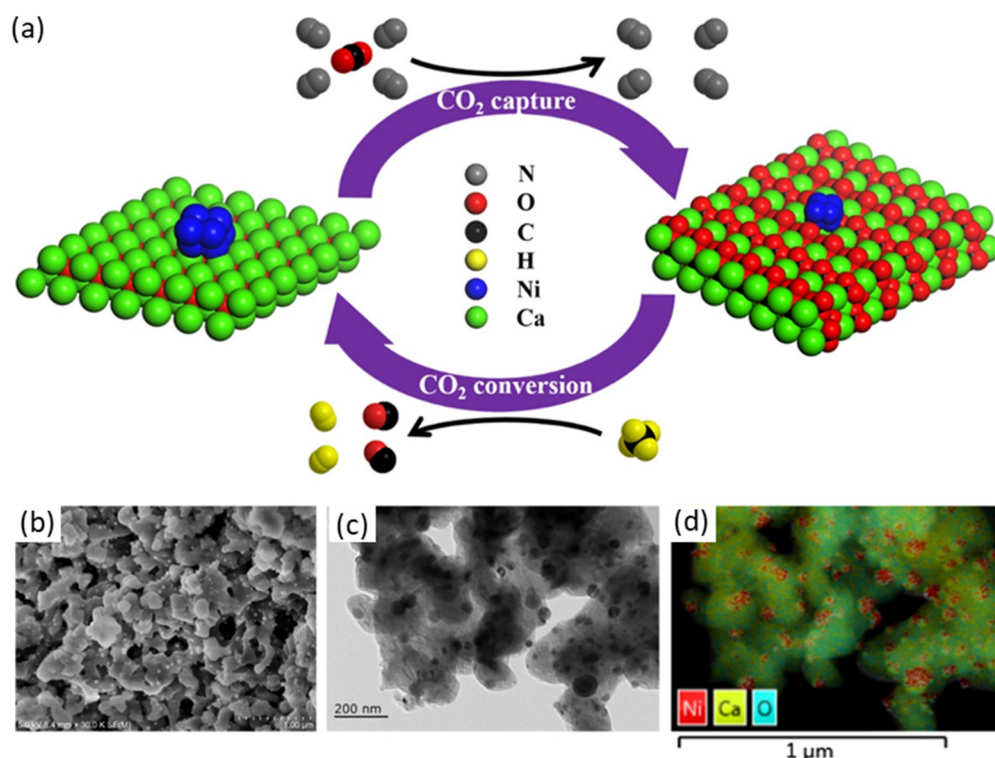
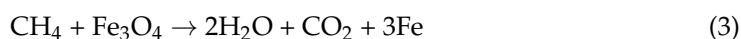


Figure 15. Illustration of the combined calcium looping and dry reforming process. (a) Process schematic, (b) particle shape and (c,d) structure and element map of the CaO-Ni multifunctional material (reduced CaO/Ni) [83].

Another example of functional chemical looping development is found in coupling CO_2 sorption to oxygen storage reduction/oxidation, e.g., for energy storage [84–86]. The working principle of such combined chemical looping system can be described as

“chemical charge” and “discharge” cycles (Figure 16). During reduction (“charge”), a feed of CH₄ and CO₂ is sent over a mechanical mixture of Fe₃O₄ and CaO. Methane reduces Fe₃O₄ to metallic iron, while producing surface carbon as well as CO₂, H₂O and H₂ (Equations (5) and (6)). The obtained H₂ can be used for fuel cells. In parallel, CaO is carbonated to CaCO₃ by interaction with CO₂ (Equation (7)), typically at temperatures between 600 and 700 °C [87]:



Depending on the need, the “charged” condition of the material can be preserved, or immediately put to use. For the latter case of “discharge”, it is sufficient to increase the temperature of the sample by 50–150 °C, which will trigger decomposition of CaCO₃ back into CaO and CO₂ (Equation (8)) [88]:



Simultaneously, the released CO₂ will interact with metallic iron and with carbon deposited in the first step to produce CO:



The CO that is generated can be used, e.g., in a solid oxide fuel cell (SOFC). Since CO intrinsically contains as much energy as hydrogen, it can indeed be oxidized electrochemically, $\text{CO} + \text{O}^{2-} = \text{CO}_2 + 2\text{e}^-$, to produce electricity and CO₂. The energetics of CO and H₂ oxidation, calculated from thermochemical data at 1123 K, yield similar values for the standard Gibbs free energy, i.e., -185 kJ mol^{-1} for CO₂ vs. -186 kJ mol^{-1} for H₂O. Moreover, the CO oxidation reaction is slightly more exothermic than that of H₂, i.e., -282 kJ mol^{-1} for CO₂ vs. -249 kJ mol^{-1} for H₂O, underlining the CO potential for fuel cell use.

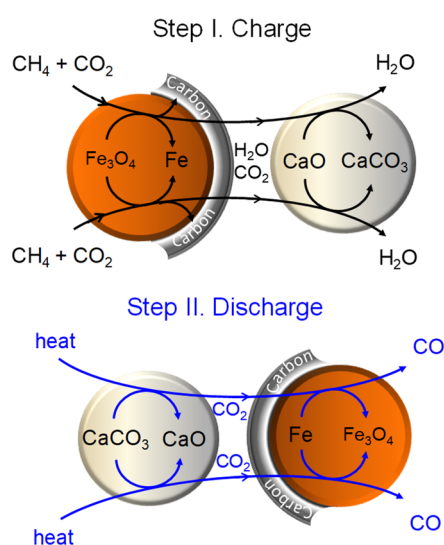


Figure 16. Illustration and working scheme of “combined chemical looping” for energy storage and conversion [84].

As exemplified before, adding a Ni catalyst can intensify the overall process. The mixture of CH₄ and CO₂ is converted to syngas over the catalyst by dry reforming. The

latter will reduce iron oxide faster and deeper than the originally fed CH_4 . Figure 17a shows space-time yields of CH_4 , CO , CO_2 and H_2 as a function of time-on-stream.

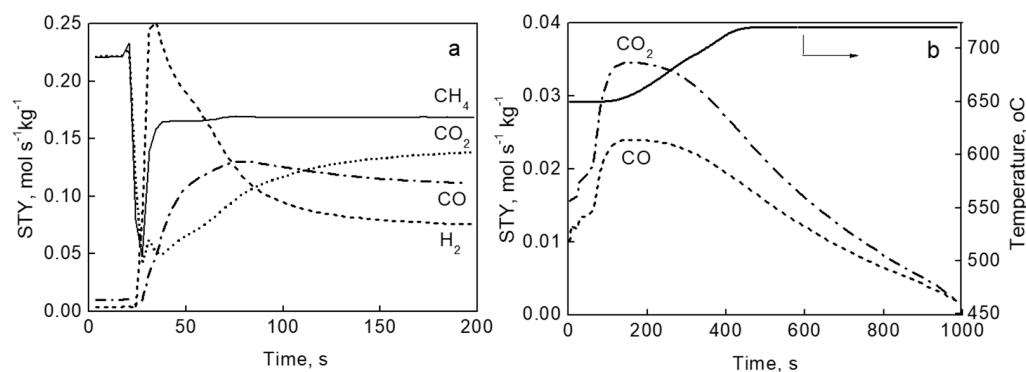


Figure 17. Space-time yield vs. time-on-stream for combined CO_2 capture and Fe_3O_4 reduction over a $\text{NiO}/\text{Fe}_2\text{O}_3\text{-CeO}_2$ and $\text{CaO-Al}_2\text{O}_3$ (1:5) mix. (a) CaO carbonation and Fe_3O_4 reduction with $\text{CH}_4 + \text{CO}_2$ (1:1) at 650°C , and (b) CaCO_3 decarbonation and CO production by iron and carbon oxidation by CO_2 . Temperature rise from 650 to 720°C in He. Solid line: temperature profile [84].

Initially, CO_2 decreases because it gets adsorbed by CaO and consumed in dry reforming. Once CaO is fully loaded with CO_2 , the CO_2 space-time yield increases again to stabilize with the other products. Due to consumption of CO_2 , CH_4 equally exhibits a minimum as it decomposes over Ni , forming surface carbon and hydrogen. The space-time yield for H_2 rises and goes through a maximum before levelling off. Fe_3O_4 gets reduced by both CO and H_2 . If needed, the process can be halted at this point to store the energy, delaying the “discharge” in time. For putting the stored energy to use, it suffices to purge the reactor with inert and raise the temperature slightly, from 650 to 720°C . This will release the CO_2 by CaCO_3 decomposition and consecutively produce CO by CO_2 oxidation of iron and carbon (Figure 17b).

This concept is widely flexible in both energy storage/release and fuel type. Dilute gas streams can be used for charging, an attractive factor for present-day applications. A further asset is that energy use or discharge and charge can easily be separated in time. Moreover, it can be merged with the newly developed solid oxide metal-air redox battery, based on oxide-ion chemistry. As such, combined chemical looping enables an emerging and promising energy storage technology, capable of harvesting renewable energy with high efficiency and of managing grid stability [89–91].

4. Conclusions

Chemical looping offers unseen opportunities for power plants and industrial applications with CO_2 capture. It is a very promising technology with large potential, well beyond combustion, and it allows to intensify processes both in fuel and chemical production technology. The flexibility of the chemical looping platform stems from the separation of a single reaction into two sub-reactions, connected by a solid carrier material. The design of suitable carrier materials is therefore key to developing novel chemical looping processes. The latter should essentially focus on acquiring understanding on how structural and compositional architecture of both the metal component and the support structure impact on the performance of the chemical looping process. Guided by this insight, catalytic sites and carrier material can be tailored to strongly enhance the process, as shown here for H_2 or CO production via methane reforming.

The principle of chemical looping is fundamentally applicable to any catalytic reaction, if suitable carriers are found that allow transport of the desired functional group. Moreover, it can be merged with existing catalytic processes for improved selectivity and stability. The inherent product separation can have a significant impact on a broad range of chemical processes, aiming for higher efficiency and ‘greener’ chemistry. We hope that this review

can trigger both experimental investigation and scientific discussions that can lead to accelerated installation of chemical looping processes.

Author Contributions: Writing-review and editing, H.P.; writing-review and editing, V.V.G. All authors have read and agreed to the published version of the manuscript.

Funding: This research received no external funding.

Conflicts of Interest: The authors declare no conflict of interest.

References

1. Davis, S.J.; Lewis, N.S.; Shaner, M.; Aggarwal, S.; Arent, D.; Azevedo, I.L.; Benson, S.M.; Bradley, T.; Brouwer, J.; Chiang, Y.-M.; et al. Net-zero emissions energy systems. *Science* **2018**, *360*, eaas9793. [[CrossRef](#)] [[PubMed](#)]
2. Martens, J.A.; Bogaerts, A.; De Kimpe, N.; Jacobs, P.A.; Marin, G.B.; Rabaey, K.; Saeys, M.; Verhelst, S. The Chemical Route to a Carbon Dioxide Neutral World. *ChemSusChem* **2017**, *10*, 1039–1055. [[CrossRef](#)]
3. Wismann, S.T.; Engbæk, J.S.; Vendelbo, S.B.; Bendixen, F.B.; Eriksen, W.L.; Aasberg-Petersen, K.; Frandsen, C.; Chorkendorff, I.; Mortensen, P.M. Electrified methane reforming: A compact approach to greener industrial hydrogen production. *Science* **2019**, *364*, 756–759. [[CrossRef](#)]
4. Vooradi, R.; Bertran, M.-O.; Frauzem, R.; Anne, S.B.; Gani, R. Sustainable chemical processing and energy-carbon dioxide management: Review of challenges and opportunities. *Chem. Eng. Res. Des.* **2018**, *131*, 440–464. [[CrossRef](#)]
5. Takht Ravanchi, M.; Sahebdehfar, S. Catalytic conversions of CO₂ to help mitigate climate change: Recent process developments. *Process. Saf. Environ. Prot.* **2021**, *145*, 172–194. [[CrossRef](#)]
6. Flores-Granobles, M.; Saeys, M. Minimizing CO₂ emissions with renewable energy: A comparative study of emerging technologies in the steel industry. *Energy Environ. Sci.* **2020**, *13*, 1923–1932. [[CrossRef](#)]
7. Abuelgasim, S.; Wang, W.; Abdalazeez, A. A brief review for chemical looping combustion as a promising CO₂ capture technology: Fundamentals and progress. *Sci. Total Environ.* **2021**, *764*, 142892. [[CrossRef](#)]
8. Zhu, X.; Imtiaz, Q.; Donat, F.; Müller, C.R.; Li, F. Chemical looping beyond combustion—A perspective. *Energy Environ. Sci.* **2020**, *13*, 772–804. [[CrossRef](#)]
9. Di Giuliano, A.; Gallucci, K. Sorption enhanced steam methane reforming based on nickel and calcium looping: A review. *Chem. Eng. Process. Process. Intensif.* **2018**, *130*, 240–252. [[CrossRef](#)]
10. Kathe, M.; Empfield, A.; Sandvik, P.; Fryer, C.; Zhang, Y.; Blair, E.; Fan, L.-S. Utilization of CO₂ as a partial substitute for methane feedstock in chemical looping methane–steam redox processes for syngas production. *Energy Environ. Sci.* **2017**, *10*, 1345–1349. [[CrossRef](#)]
11. Dang, C.; Li, Y.; Yusuf, S.M.; Cao, Y.; Wang, H.; Yu, H.; Peng, F.; Li, F. Calcium cobaltate: A phase-change catalyst for stable hydrogen production from bio-glycerol. *Energy Environ. Sci.* **2018**, *11*, 660–668. [[CrossRef](#)]
12. Zhao, X.; Zhou, H.; Sikarwar, V.S.; Zhao, M.; Park, A.-H.A.; Fennell, P.S.; Shen, L.; Fan, L.-S. Biomass-based chemical looping technologies: The good, the bad and the future. *Energy Environ. Sci.* **2017**, *10*, 1885–1910. [[CrossRef](#)]
13. Zeng, L.; Cheng, Z.; Fan, J.A.; Fan, L.-S.; Gong, J. Metal oxide redox chemistry for chemical looping processes. *Nat. Rev. Chem.* **2018**, *2*, 349–364. [[CrossRef](#)]
14. Li, D.; Xu, R.; Li, X.; Li, Z.; Zhu, X.; Li, K. Chemical Looping Conversion of Gaseous and Liquid Fuels for Chemical Production: A Review. *Energy Fuels* **2020**, *34*, 5381–5413. [[CrossRef](#)]
15. Adanez, J.; Abad, A.; Garcia-Labiano, F.; Gayan, P.; De Diego, L.F. Progress in Chemical-Looping Combustion and Reforming technologies. *Prog. Energy Combust. Sci.* **2012**, *38*, 215–282. [[CrossRef](#)]
16. Fan, L.-S.; Zeng, L.; Luo, S. Chemical-looping technology platform. *AIChE J.* **2014**, *61*, 2–22. [[CrossRef](#)]
17. Yan, X.; Li, Y.; Ma, X.; Zhao, J.; Wang, Z. Performance of Li₄SiO₄ material for CO₂ capture: A review. *Int. J. Mol. Sci.* **2019**, *20*, 928. [[CrossRef](#)]
18. Kim, S.M.; Abdala, P.M.; Broda, M.; Hosseini, D.; Copéret, C.; Müller, C. Integrated CO₂ Capture and Conversion as an Efficient Process for Fuels from Greenhouse Gases. *ACS Catal.* **2018**, *8*, 2815–2823. [[CrossRef](#)]
19. Fan, L.-S. *Chemical Looping Systems for Fossil Energy Conversions*; John Wiley and Sons Inc.: Hoboken, NJ, USA, 2010.
20. Criado, Y.A.; Arias, B.; Abanades, J.C. Calcium looping CO₂ capture system for back-up power plants. *Energy Environ. Sci.* **2017**, *10*, 1994–2004. [[CrossRef](#)]
21. Blamey, J.; Anthony, E.J.; Wang, J.; Fennell, P.S. The calcium looping cycle for large-scale CO₂ capture. *Prog. Energy Combust. Sci.* **2010**, *36*, 260–279. [[CrossRef](#)]
22. Tian, H.; Simonyi, T.; Poston, J.; Siriwardane, R. Effect of Hydrogen Sulfide on Chemical Looping Combustion of Coal-Derived Synthesis Gas over Bentonite-Supported Metal–Oxide Oxygen Carriers. *Ind. Eng. Chem. Res.* **2009**, *48*, 8418–8430. [[CrossRef](#)]
23. Kane, T.; Guerrero Caballero, J.; Löfberg, A. Chemical looping selective oxidation of H₂S using V₂O₅ impregnated over different supports as oxygen carriers. *ChemCatChem* **2020**, *12*, 2569–2579. [[CrossRef](#)]
24. Zhu, J.; Sushkevich, V.L.; Knorpp, A.J.; Newton, M.A.; Mizuno, S.C.M.; Wakihara, T.; Okubo, T.; Liu, Z.; Van Bokhoven, J.A. Cu-Erionite Zeolite Achieves High Yield in Direct Oxidation of Methane to Methanol by Isothermal Chemical Looping. *Chem. Mater.* **2020**, *32*, 1448–1453. [[CrossRef](#)]

25. Ishida, M.; Zheng, D.; Akehata, T. Evaluation of a chemical-looping-combustion power-generation system by graphic exergy analysis. *Energy* **1987**, *12*, 147–154. [[CrossRef](#)]
26. Richter, H.J.; Knoche, K.F. Reversibility of Combustion Processes. *ACS Symp. Ser.* **1983**, *235*, 71–85. [[CrossRef](#)]
27. Mattisson, T.; Keller, M.; Linderholm, C.; Moldenhauer, P.; Rydén, M.; Leion, H.; Lyngfelt, A. Chemical-looping technologies using circulating fluidized bed systems: Status of development. *Fuel Process. Technol.* **2018**, *172*, 1–12. [[CrossRef](#)]
28. Huang, J.; Liu, W.; Yang, Y.; Liu, B. High-Performance Ni–Fe Redox Catalysts for Selective CH₄ to Syngas Conversion via Chemical Looping. *ACS Catal.* **2018**, *8*, 1748–1756. [[CrossRef](#)]
29. Mihai, O.; Chen, D.; Holmén, A. Catalytic Consequence of Oxygen of Lanthanum Ferrite Perovskite in Chemical Looping Reforming of Methane. *Ind. Eng. Chem. Res.* **2011**, *50*, 2613–2621. [[CrossRef](#)]
30. Lyngfelt, A. Oxygen Carriers for Chemical-Looping Combustion. In *Calcium and Chemical Looping Technology for Power Generation and Carbon Dioxide (CO₂) Capture*; Fennell, P., Anthony, B., Eds.; Woodhead Publishing: Cambridge, UK, 2015; Chapter 11; pp. 221–254.
31. Solunke, R.D.; Vesper, G. Integrating desulfurization with CO₂-capture in chemical-looping combustion. *Fuel* **2011**, *90*, 608–617. [[CrossRef](#)]
32. Dou, Y.; Sun, L.; Ren, J.; Dong, L. Opportunities and future challenges in hydrogen economy for sustainable development. In *Hydrogen Economy*; Scipioni, A., Manzardo, A., Ren, J., Eds.; Academic Press: Cambridge, MA, USA, 2017; Chapter 10; pp. 277–305.
33. Nehrir, M.H.; Wang, C. Fuel cells. In *Electric Renewable Energy Systems*; Rashid, M.H., Ed.; Academic Press: Boston, MA, USA, 2016; Chapter 6; pp. 92–113.
34. Song, C. Fuel processing for low-temperature and high-temperature fuel cells Challenges, and opportunities for sustainable development in the 21st century. *Catal. Today* **2002**, *77*, 17–49. [[CrossRef](#)]
35. Choudhary, T.V.; Goodman, D.W. Co-free fuel processing for fuel cell applications. *Catal. Today* **2002**, *77*, 65–78. [[CrossRef](#)]
36. Liu, W.; Lim, J.Y.; Saucedo, M.A.; Hayhurst, A.N.; Scott, S.A.; Dennis, J. Kinetics of the reduction of wüstite by hydrogen and carbon monoxide for the chemical looping production of hydrogen. *Chem. Eng. Sci.* **2014**, *120*, 149–166. [[CrossRef](#)]
37. Galvita, V.; Sundmacher, K. Cyclic water gas shift reactor (CWGS) for carbon monoxide removal from hydrogen feed gas for PEM fuel cells. *Chem. Eng. J.* **2007**, *134*, 168–174. [[CrossRef](#)]
38. Buelens, L.C.; Galvita, V.V.; Poelman, H.; Detavernier, C.; Marin, G.B. Super-dry reforming of methane intensifies CO₂ utilization via le chatelier’s principle. *Science* **2016**, *354*, 449–452. [[CrossRef](#)]
39. Galvita, V.V.; Poelman, H.; Marin, G.B. Hydrogen Production from Methane and Carbon Dioxide by Catalyst-Assisted Chemical Looping. *Top. Catal.* **2011**, *54*, 907–913. [[CrossRef](#)]
40. Najera, M.; Solunke, R.; Gardner, T.; Vesper, G. Carbon capture and utilization via chemical looping dry reforming. *Chem. Eng. Res. Des.* **2011**, *89*, 1533–1543. [[CrossRef](#)]
41. Bhavsar, S.; Nájera, M.; Vesper, G. Chemical Looping Dry Reforming as Novel, Intensified Process for CO₂ Activation. *Chem. Eng. Technol.* **2012**, *35*, 1281–1290. [[CrossRef](#)]
42. Hu, J.; Galvita, V.V.; Poelman, H.; Marin, G.B. Advanced Chemical Looping Materials for CO₂ Utilization: A Review. *Materials* **2018**, *11*, 1187. [[CrossRef](#)]
43. Loutzenhiser, P.G.; Gálvez, M.E.; Hischer, I.; Stamatou, A.; Frei, A.; Steinfeld, A. CO₂ splitting via two-step solar thermo-chemical cycles with zn/zno and FeO/Fe₃O₄ redox reactions ii: Kinetic analysis. *Energy Fuels* **2009**, *23*, 2832–2839. [[CrossRef](#)]
44. Galvita, V.; Hempel, T.; Lorenz, H.; Rihko-Struckmann, L.K.; Sundmacher, K. Deactivation of Modified Iron Oxide Materials in the Cyclic Water Gas Shift Process for CO-Free Hydrogen Production. *Ind. Eng. Chem. Res.* **2008**, *47*, 303–310. [[CrossRef](#)]
45. Theofanidis, S.A.; Galvita, V.V.; Poelman, H.; Marin, G.B. Enhanced Carbon-Resistant Dry Reforming Fe-Ni Catalyst: Role of Fe. *ACS Catal.* **2015**, *5*, 3028–3039. [[CrossRef](#)]
46. Daza, C.E.; Kiennemann, A.; Moreno, S.; Molina, R. Dry reforming of methane using Ni–Ce catalysts supported on a modified mineral clay. *Appl. Catal. A Gen.* **2009**, *364*, 65–74. [[CrossRef](#)]
47. Potdar, H.S.; Roh, H.-S.; Jun, K.-W.; Ji, M.; Liu, Z.-W. Carbon dioxide reforming of methane over co-precipitated Ni-Ce-ZrO₂ catalysts. *Catal. Lett.* **2002**, *84*, 95–100.
48. Galvita, V.V.; Poelman, H.; Detavernier, C.; Marin, G.B. Catalyst-assisted chemical looping for CO₂ conversion to CO. *Appl. Catal. B Environ.* **2015**, *164*, 184–191. [[CrossRef](#)]
49. Yin, X.; Wang, S.; Sun, R.; Jiang, S.; Shen, L.-H. A Ce–Fe Oxygen Carrier with a Core–Shell Structure for Chemical Looping Steam Methane Reforming. *Ind. Eng. Chem. Res.* **2020**, *59*, 9775–9786. [[CrossRef](#)]
50. Galinsky, N.L.; Shafiefarhood, A.; Chen, Y.; Neal, L.; Li, F. Effect of support on redox stability of iron oxide for chemical looping conversion of methane. *Appl. Catal. B Environ.* **2015**, *164*, 371–379. [[CrossRef](#)]
51. Tang, M.; Xu, L.; Fan, M. Progress in oxygen carrier development of methane-based chemical-looping reforming: A review. *Appl. Energy* **2015**, *151*, 143–156. [[CrossRef](#)]
52. Zhu, X.; Li, K.; Wei, Y.; Wang, H.; Sun, L. Chemical-Looping Steam Methane Reforming over a CeO₂–Fe₂O₃ Oxygen Carrier: Evolution of Its Structure and Reducibility. *Energy Fuels* **2014**, *28*, 754–760. [[CrossRef](#)]
53. Galvita, V.V.; Poelman, H.; Bliznuk, V.; Detavernier, C.; Marin, G.B. CeO₂-modified Fe₂O₃ for CO₂ utilization via chemical looping. *Ind. Eng. Chem. Res.* **2013**, *52*, 8416–8426. [[CrossRef](#)]

54. Dharanipragada, N.V.R.A.; Meledina, M.; Galvita, V.V.; Poelman, H.; Turner, S.; Van Tendeloo, G.; Detavernier, C.; Marin, G.B. Deactivation Study of $\text{Fe}_2\text{O}_3\text{-CeO}_2$ during Redox Cycles for CO Production from CO_2 . *Ind. Eng. Chem. Res.* **2016**, *55*, 5911–5922. [[CrossRef](#)]
55. Dharanipragada, N.A.; Galvita, V.V.; Poelman, H.; Buelens, L.C.; Detavernier, C.; Marin, G.B. Bifunctional Co- and Ni-ferrites for catalyst-assisted chemical looping with alcohols. *Appl. Catal. B Environ.* **2018**, *222*, 59–72. [[CrossRef](#)]
56. Hu, J.; Buelens, L.; Theofanidis, S.-A.; Galvita, V.V.; Poelman, H.; Marin, G.B. CO_2 conversion to CO by autothermal catalyst-assisted chemical looping. *J. CO₂ Util.* **2016**, *16*, 8–16. [[CrossRef](#)]
57. Sun, Z.; Chen, S.; Hu, J.; Chen, A.; Rony, A.H.; Russell, C.K.; Xiang, W.; Fan, M.; Dyar, M.D.; Dklute, E.C. $\text{Ca}_2\text{Fe}_2\text{O}_5$: A promising oxygen carrier for CO/ CH_4 conversion and almost-pure H_2 production with inherent CO_2 capture over a two-step chemical looping hydrogen generation process. *Appl. Energy* **2018**, *211*, 431–442. [[CrossRef](#)]
58. Liu, S.; Xiang, D.; Xu, Y.; Sun, Z.; Cao, Y. Relationship between electronic properties of Fe_3O_4 substituted by Ca and Ba and their reactivity in chemical looping process: A first-principles study. *Appl. Energy* **2017**, *202*, 550–557. [[CrossRef](#)]
59. Chan, M.S.; Liu, W.; Ismail, M.; Yang, Y.; Scott, S.A.; Dennis, J.S. Improving hydrogen yields, and hydrogen:steam ratio in the chemical looping production of hydrogen using $\text{Ca}_2\text{Fe}_2\text{O}_5$. *Chem. Eng. J.* **2016**, *296*, 406–411. [[CrossRef](#)]
60. Sun, Z.; Chen, S.; Russell, C.K.; Hu, J.; Rony, A.H.; Tan, G.; Chen, A.; Duan, L.; Boman, J.; Tang, J.; et al. Improvement of H_2 -rich gas production with tar abatement from pine wood conversion over bi-functional $\text{Ca}_2\text{Fe}_2\text{O}_5$ catalyst: Investigation of inner-looping redox reaction and promoting mechanisms. *Appl. Energy* **2018**, *212*, 931–943. [[CrossRef](#)]
61. Hosseini, D.; Donat, F.; Abdala, P.M.; Kim, S.M.; Kierzkowska, A.M.; Müller, C.R. Reversible Exsolution of Dopant Improves the Performance of $\text{Ca}_2\text{Fe}_2\text{O}_5$ for Chemical Looping Hydrogen Production. *ACS Appl. Mater. Interfaces* **2019**, *11*, 18276–18284. [[CrossRef](#)]
62. Carrillo, A.J.; Kim, K.J.; Hood, Z.D.; Bork, A.H.; Rupp, J.L.M. $\text{La}_{0.6}\text{Sr}_{0.4}\text{Cr}_{0.8}\text{Co}_{0.2}\text{O}_3$ Perovskite Decorated with Exsolved Co Nanoparticles for Stable CO_2 Splitting and Syngas Production. *ACS Appl. Energy Mater.* **2020**, *3*, 4569–4579. [[CrossRef](#)]
63. Kousi, K.; Neagu, D.; Bekris, L.; Papaioannou, E.I.; Metcalfe, I.S. Endogenous Nanoparticles Strain Perovskite Host Lattice Providing Oxygen Capacity and Driving Oxygen Exchange and CH_4 Conversion to Syngas. *Angew. Chem. Int. Ed.* **2019**, *59*, 2510–2519. [[CrossRef](#)]
64. Otto, S.-K.; Kousi, K.; Neagu, D.; Bekris, L.; Janek, J.; Metcalfe, I.S. Exsolved Nickel Nanoparticles Acting as Oxygen Storage Reservoirs and Active Sites for Redox CH_4 Conversion. *ACS Appl. Energy Mater.* **2019**, *2*, 7288–7298. [[CrossRef](#)]
65. Gärtner, C.A.; van Veen, A.C.; Lercher, J.A. Oxidative dehydrogenation of ethane: Common principles and mechanistic aspects. *ChemCatChem* **2013**, *5*, 3196–3217. [[CrossRef](#)]
66. Bañares, M.A. Supported metal oxide and other catalysts for ethane conversion: A review. *Catal. Today* **1999**, *51*, 319–348. [[CrossRef](#)]
67. Nowicka, E.; Reece, C.; Althahban, S.M.; Mohammed, K.M.H.; Kondrat, S.A.; Morgan, D.J.; He, Q.; Willock, D.J.; Golunski, S.; Kiely, C.J.; et al. Elucidating the Role of CO_2 in the Soft Oxidative Dehydrogenation of Propane over Ceria-Based Catalysts. *ACS Catal.* **2018**, *8*, 3454–3468. [[CrossRef](#)]
68. Gao, Y.; Haeri, F.; He, F.; Li, F. Alkali metal-promoted $\text{La}_x\text{Sr}_{2-x}\text{FeO}_{4-\delta}$ redox catalysts for chemical looping oxidative dehydrogenation of ethane. *ACS Catal.* **2018**, *8*, 1757–1766. [[CrossRef](#)]
69. Yusuf, S.; Neal, L.; Bao, Z.; Wu, Z.; Li, F. Effects of sodium and tungsten promoters on mg_6mno_8 -based core-shell redox catalysts for chemical looping—oxidative dehydrogenation of ethane. *ACS Catal.* **2019**, *9*, 3174–3186. [[CrossRef](#)]
70. Galinsky, N.; Sendi, M.; Bowers, L.; Li, F. $\text{CaMn}_{1-x}\text{B}_x\text{O}_3-\delta$ (b=Al, V, Fe, Co and Ni) perovskite based oxygen carriers for chemical looping with oxygen uncoupling (clou). *Appl. Energy* **2016**, *174*, 80–87. [[CrossRef](#)]
71. Kang, D.; Lim, H.S.; Lee, M.; Lee, J.W. Syngas production on a Ni-enhanced $\text{Fe}_2\text{O}_3/\text{Al}_2\text{O}_3$ oxygen carrier via chemical looping partial oxidation with dry reforming of methane. *Appl. Energy* **2018**, *211*, 174–186. [[CrossRef](#)]
72. Brady, C.; Murphy, B.; Xu, B. Enhanced methane dehydroaromatization via coupling with chemical looping. *ACS Catal.* **2017**, *7*, 3924–3928. [[CrossRef](#)]
73. Zhang, X.; Pei, C.; Chang, X.; Chen, S.; Liu, R.; Zhao, Z.-J.; Mu, R.; Gong, J. FeO_6 Octahedral Distortion Activates Lattice Oxygen in Perovskite Ferrite for Methane Partial Oxidation Coupled with CO_2 Splitting. *J. Am. Chem. Soc.* **2020**, *142*, 11540–11549. [[CrossRef](#)] [[PubMed](#)]
74. Gao, W.; Guo, J.; Wang, P.; Wang, Q.; Chang, F.; Pei, Q.; Zhang, W.; Liu, L.; Chen, P. Production of ammonia via a chemical looping process based on metal imides as nitrogen carriers. *Nat. Energy* **2018**, *3*, 1067–1075. [[CrossRef](#)]
75. Lyon, R.K.; Cole, J.A. Unmixed combustion: An alternative to fire. *Combust. Flame* **2000**, *121*, 249–261. [[CrossRef](#)]
76. Martavaltzi, C.S.; Lemonidou, A.A. Development of new CaO based sorbent materials for CO_2 removal at high temperature. *Microporous Mesoporous Mater.* **2008**, *110*, 119–127. [[CrossRef](#)]
77. Fernández, J.; Abanades, J. Optimized design and operation strategy of a CaCu chemical looping process for hydrogen production. *Chem. Eng. Sci.* **2017**, *166*, 144–160. [[CrossRef](#)]
78. Antzara, A.; Heracleous, E.; Bukur, D.B.; Lemonidou, A. Thermodynamic analysis of hydrogen production via chemical looping steam methane reforming coupled with in situ CO_2 capture. *Int. J. Greenh. Gas Control.* **2015**, *32*, 115–128. [[CrossRef](#)]
79. Martavaltzi, C.S.; Pampaka, E.P.; Korkakaki, E.S.; Lemonidou, A.A. Hydrogen Production via Steam Reforming of Methane with Simultaneous CO_2 Capture over $\text{CaO-Ca}_{12}\text{Al}_{14}\text{O}_{33}$. *Energy Fuels* **2010**, *24*, 2589–2595. [[CrossRef](#)]

80. Antzara, A.; Heracleous, E.; Lemonidou, A.A. Energy efficient sorption enhanced-chemical looping methane reforming process for high-purity H₂ production: Experimental proof-of-concept. *Appl. Energy* **2016**, *180*, 457–471. [[CrossRef](#)]
81. Li, H.; Dang, C.; Yang, G.; Cao, Y.; Wang, H.; Peng, F.; Yu, H. Bi-functional particles for integrated thermo-chemical processes: Catalysis and beyond. *Particuology* **2021**. [[CrossRef](#)]
82. Verbeeck, K.; Buelens, L.C.; Galvita, V.V.; Marin, G.B.; Van Geem, K.M.; Rabaey, K. Upgrading the value of anaerobic digestion via chemical production from grid injected biomethane. *Energy Environ. Sci.* **2018**, *11*, 1788–1802.
83. Tian, S.; Yan, F.; Zhang, Z.; Jiang, J. Calcium-looping reforming of methane realizes in situ CO₂ utilization with improved energy efficiency. *Sci. Adv.* **2019**, *5*, eaav5077. [[CrossRef](#)] [[PubMed](#)]
84. Galvita, V.V.; Poelman, H.; Marin, G.B. Combined chemical looping for energy storage and conversion. *J. Power Sources* **2015**, *286*, 362–370. [[CrossRef](#)]
85. Galvita, V.V.; Poelman, H.; Marin, G.B. Combined Chemical Looping: New Possibilities for Energy Storage and Conversion. *Energy Fuels* **2017**, *31*, 11509–11514. [[CrossRef](#)]
86. Saghafifar, M.; Schnellmann, M.A.; Scott, S.A. Chemical looping electricity storage. *Appl. Energy* **2020**, *279*, 115553. [[CrossRef](#)]
87. Abanades, J.C.; Alvarez, D. Conversion limits in the reaction of CO₂ with lime. *Energy Fuels* **2003**, *17*, 308–315. [[CrossRef](#)]
88. Vorrias, I.; Atsonios, K.; Nikolopoulos, A.; Nikolopoulos, N.; Grammelis, P.; Kakaras, E. Calcium looping for CO₂ capture from a lignite fired power plant. *Fuel* **2013**, *113*, 826–836. [[CrossRef](#)]
89. Zhang, C.; Huang, K. A comprehensive review on the development of solid-state metal–air batteries operated on oxide-ion chemistry. *Adv. Energy Mater.* **2021**, *11*, 2000630. [[CrossRef](#)]
90. Xu, N.; Li, X.; Zhao, X.; Goodenough, J.B.; Huang, K. A novel solid oxide redox flow battery for grid energy storage. *Energy Environ. Sci.* **2011**, *4*, 4942–4946. [[CrossRef](#)]
91. Menzler, N.H.; Hospach, A.; Niewolak, L.; Bram, M.; Tokariev, O.; Berger, C.M.; Orzessek, P.; Quadackers, W.J.; Fang, Q.; Buchkremer, H.P. Power-To-Storage—The Use of an Anode-Supported Solid Oxide Fuel Cell as a High-Temperature Battery. *ECS Trans.* **2013**, *57*, 255–267. [[CrossRef](#)]